

# Ultrahigh Photocatalytic CO<sub>2</sub> Reduction Efficiency by Single Metallic Atom Oxide on TiO<sub>2</sub>

**Yibo Feng**

Beijing University of Technology

**Cong Wang**

Beijing University of Technology

**Peixin Cui**

Institute of Soil Science, Chinese Academy of Sciences <https://orcid.org/0000-0002-9887-2784>

**Chong Li**

Zhengzhou University

**Liyong Gan**

Chongqing University

**Shengbai Zhang**

Rensselaer Polytechnic Institute

**Xiaoyuan Zhou**

Chongqing University

**Xiaoxian Zhang**

Beijing Jiaotong University

**Hui Li**

Beijing University of Technology

**Kaiwen Wang**

Beijing University of Technology

**Zhiming Sun**

Beijing University of Technology

**Kai Zhou**

Chongqing University

**Bin Zhang**

Chongqing University

**Min Li**

China University of Geosciences

**Hongwei Huang**

China University of Geosciences

**Wei Li**

Beijing University of Technology

**Ang Li**

Beijing University of Technology

**Lihua Wang**

Beijing University of Technology

**JunHuang**

Beijing University of Technology

**Ze Zhang**

Zhejiang University

**Xiaodong Han** (✉ [xdhan@bjut.edu.cn](mailto:xdhan@bjut.edu.cn))

Beijing Key Laboratory of Microstructure and Property of Advanced Materials, Beijing University of Technology, 100124 Beijing, China.

---

## Article

**Keywords:** Adatom at step, TiO<sub>2</sub>, Single Metallic Atom Oxides, CO<sub>2</sub> reduction, Photocatalyst

**Posted Date:** November 9th, 2020

**DOI:** <https://doi.org/10.21203/rs.3.rs-91974/v1>

**License:** © ⓘ This work is licensed under a Creative Commons Attribution 4.0 International License.

[Read Full License](#)

---

# Abstract

Photocatalytic carbon dioxide ( $\text{CO}_2$ ) reduction is a sustainable and energy-consumption-free route to directly convert the greenhouse gas into chemicals. Given the vast amount of greenhouse gases, numerous efforts have been devoted to developing inorganic photocatalysts due to their stable, low-cost and environmental-friendly properties. However, more efficient titanium dioxide ( $\text{TiO}_2$ ) without noble metal or sacrifice/organic agent is highly desirable for  $\text{CO}_2$  reduction practical application, and it is also difficult and urgently in demand for  $\text{TiO}_2$  producing selectively valuable compounds, i.e. industrial chemicals and fuels. Here, we develop a novel “adatom at step” strategy via anchoring single tungsten atom oxide (STAO) site on intrinsic steps of classic  $\text{TiO}_2$  nanoparticles. The composition of single-sites can be controlled by tuning the ratio of adatom  $\text{W}^{5+}$  to neighboring  $\text{Ti}^{3+}$ , resulting in significant  $\text{CO}_2$  reduction efficiency and selectively yield of carbon monoxide (CO) or methane ( $\text{CH}_4$ ) as main products. The  $\text{W}^{5+}$ -dominated catalysts can achieve an ultrahigh photocatalytic  $\text{CH}_4$  production of  $59.3 \mu\text{mol/g/h}$ , while the  $\text{Ti}^{3+}$ -dominated catalysts can achieve a CO production of  $181.4 \mu\text{mol/g/h}$ , which both exceed those of pristine  $\text{TiO}_2$  by more than one order of magnitude. The mechanism relies on the accurate control of atomic sites with high coverage and the subsequent excellent electron-hole separation along with favorable adsorption-desorption of intermediates on sites. This approach not only provides a novel strategy for inorganic catalytic single-sites with superior performance, but also identifies the rational design mechanisms of the efficient site with controllable production.

# Introduction

Carbon fuel consumption and  $\text{CO}_2$  greenhouse gas emissions are imperative for the sustainable development of human civilization, causing acceleration of energy shortages and global warming [1-5]. The photocatalytic  $\text{CO}_2$  reduction reaction has been considered an environmentally friendly method to “kill two birds with one stone” in the conversion of  $\text{CO}_2$  for carbon fuel technologies [7-11]. In recent years, numerous catalysts have been widely studied to improve the efficiency and selectivity of this reaction in a variety of products, such as carbon monoxide (CO), methanol ( $\text{CH}_3\text{OH}$ ) and methane ( $\text{CH}_4$ ) [12-18]. As low-cost, stable and eco-friendly candidates, inorganic metal oxides have attracted tremendous interest in photocatalytic  $\text{CO}_2$  reduction [19-25]. The exploration of high performance metal oxide photocatalysts in  $\text{CO}_2$  reduction reaction is highly desired. Among them, titanium dioxide ( $\text{TiO}_2$ ) is the most extensively-investigated photocatalyst due to its beneficial band diagram, non-toxicity and photoactivity [26-36]. Compared with hybrid photocatalytic systems with high reactivity, i.e. homogeneous molecular catalysts [37-41] and organic framework-based catalysts [42-46], pristine  $\text{TiO}_2$  heterogeneous catalysts still present obstacles in general strategies of improving photocatalytic  $\text{CO}_2$  efficiency and uncontrollable selectivity.

The mechanism of catalytically active sites is highly important to promote photocatalytic  $\text{CO}_2$  reduction activity and particularly product selectivity. In the process of photocatalytic  $\text{CO}_2$  reduction on  $\text{TiO}_2$ , the electrons are generated by light irradiation and then transferred to the catalytically active sites to react

with the adsorbed  $\text{CO}_2$  molecules. Consequently, there are three main aspects to improving  $\text{TiO}_2$ -based catalytic efficiency, namely including **(1)** intrinsic light absorption, **(2)** kinetic photocarrier transfer pathway and **(3)** intermediates adsorption-desorption and hydrogenation. Tremendous efforts have been made to optimize photocarrier separation and charge transfer pathway on  $\text{TiO}_2$ . Recently for instance, a  $\text{TiO}_2$ -graphene composite structure was found to improve high surface area for  $\text{CO}_2$  adsorption and increase the anatase- $\text{TiO}_2$  light absorption region, resulting in increasing  $\text{CO}_2$  reduction efficiency. [28] Surface vacancy-mediated  $\text{Ti}^{3+}$  in  $\text{TiO}_2$  can efficiently accelerate the adsorption and chemical activation of  $\text{CO}_2$ . [29] In general, synergistic effect of these three aspects is important and stringent. Besides, these aspects also influence each other.  $\text{Ag}/\text{TiO}_2$  shows a strong interfacial coupling leading to an efficient separation of photogenerated carriers and a consequent enhanced selectivity between  $\text{CH}_4$  and  $\text{CH}_3\text{OH}$ . [30] Additionally, note that the hydrogenation of  $\text{CO}_2$  plays a vital role in the design of thermocatalysts [16], rational design of active sites on photocatalysts are needed to further explored to accelerate  $\text{CO}_2$  reduction. However, these inorganic  $\text{TiO}_2$ -based photocatalytic performance are still not sufficient for the practical applications. Meanwhile, owing to the lack of in-depth understanding of photocatalytic active sites at the atomic scale, most of the  $\text{TiO}_2$  catalysts still suffer from non-controllable products (a  $\text{C}_1$  mixture containing  $\text{CO}$ ,  $\text{CH}_4$  and  $\text{CH}_3\text{OH}$ ).

With the blooming development of single-atom catalysts and accurate atomic site configuration on catalysts, numerous active sites with controllable products have been investigated and gradually recognized by creating single-sites or introducing co-catalysts or dimer reactive sites [47-59], e. g. in thermo- and electro-catalytic active sites rational design, both isolated sites and the proper atomic configuration of supports are of great importance for  $\text{CO}_2$  reduction activity, stability and selectivity [52]. In photocatalytic hydrogenation of  $\text{C}=\text{O}$ ,  $\text{Cu-In}$  dimer atomic sites have been found to promote the  $\text{CH}_4$  production with almost 100% selectivity [56]. Thus, a thorough study of atomic-scale configuration on  $\text{TiO}_2$  should be undoubtedly applied to enhance the efficiency and selectivity via controlling hydrogenation process. In recent years, the atomic-scale configurations of single-sites have been developed, i. e. single-atom, single-metal-atom-oxide and single-unit-cell [60-63]. Following this route for  $\text{TiO}_2$ , potential active sites can be designed as a single site anchored on  $\text{TiO}_2$  surface [64-75], and atomic step site on  $\text{TiO}_2$  has been verified to enhance electron-transfer and molecular capture capability [76-80]. However, as the most common intrinsic defects on  $\text{TiO}_2$  surfaces and probably the predominant ones on  $\text{TiO}_2$  nanoparticles [81, 82], atomic steps on  $\text{TiO}_2$  surface has never been reported as adatom substrate for single-sites anchoring. Therefore, it is imperative to explore single-site anchoring strategy at the atomic  $\text{TiO}_2$  steps to realize high efficient  $\text{CO}_2$  reduction via further optimizing the photocarrier separation and reaction pathway.

Herein, we develop single-tungsten-atom oxide (STAO) on  $\text{TiO}_2$  (101) terrace edges, i.e. an oxygen-coordinated tungsten atom ( $\text{W}^{5+}$ ) anchored at  $\text{TiO}_2$  atomic steps. The facile method of “adatom at step” can not only create novel active sites via anchoring single-atoms at steps, but also cause neighboring

Ti<sup>3+</sup> formation. The rational design strategy of “adatom at step” is schematically illustrated in **Figure 1a**. The densities of single W<sup>5+</sup> and Ti<sup>3+</sup> sites are optimized to achieve W<sup>5+</sup>- and Ti<sup>3+</sup>-dominant catalysts, yielding superior CH<sub>4</sub> and CO production with high selectivity, respectively. The controlled CH<sub>4</sub> production efficiency is highest one compared with other photocatalysts without noble-metal. Due to the variation of adatom elements and oxygen coordination, there exists a larger number of “adatom at step” sites for rational design and new mechanisms with exceptional catalytic performance could be uncovered.

## Results And Discussions

### Structural characterization of STAO at TiO<sub>2</sub> atomic steps

The atomic morphology of STAO at step sites is illustrated via Cs-corrected scanning transmission electron microscopy high-angle annular dark field (STEM-HAADF), indicating the STAO bright spot uniformly dispersed on TiO<sub>2</sub> nanoparticles (Fig. 1b). The elemental mapping analysis confirms that tungsten (W), titanium (Ti) and oxygen (O) are evenly dispersed (Fig. 1c). Moreover, Fig. 1b clearly demonstrates that W atoms are anchored above the vertical centers of Ti atoms, suggesting STAO sites are deposited at the steps with certain distortion as demonstrated in Fig. 1a. Since monoatomic-height steps at terraces constitute the most common defects on TiO<sub>2</sub> nanoparticle surface, chemical adsorption or new sites nucleation are more accessible at steps on metal oxide surfaces [76-82]. As shown in Figure S1, the step of TiO<sub>2</sub> nanoparticles (approximately 5-10 nm) are identified mainly on (101) terrace in HAADF results. Furthermore, steps can be identified as mono- or bi-atomic steps at the edge of (101) terrace based on statistic of steps density in HAADF images (Fig. S1).

Since the amount of steps is sufficient on TiO<sub>2</sub> surface, the density of the anchored STAO at steps can be controlled via depositing various STAO concentration, determined by inductively coupled plasma optical emission spectrometry (ICP-OES). It is found that the maximum tungsten density on TiO<sub>2</sub> can reach 3 wt% (Table S1). When considering the anchored STAO as a quasi-spherical model, the maximum number of W atoms covering on TiO<sub>2</sub> (101) surface is calculated as 8% approximately. Images of low-coverage (0.1%) and high-coverage (8%) STAO sites anchored on TiO<sub>2</sub> are presented in Figure S2.

To confirm the valence state of STAO sites at TiO<sub>2</sub> steps and their influence on TiO<sub>2</sub> substrate, X-ray photoelectron spectroscopy (XPS) characterization was performed. Firstly for the uniformly dispersed tungsten, main peaks appearing as shoulders at 34.7 eV (W<sub>4f7/2</sub>) and 36.7 eV (W<sub>4f5/2</sub>) can be identified to the W<sup>5+</sup> doublet, while the peaks at 35.8 eV (W<sub>4f7/2</sub>) and 37.8 eV (W<sub>4f5/2</sub>) are due to the W<sup>6+</sup> doublet (Fig. 1d) [63]. It can be noticed that the majority of W on TiO<sub>2</sub> surface exhibit 5+ valence state. Besides, Ti<sub>2p</sub> banding energy (Fig. 1e) shows a down-shift of 0.5 eV compared with pristine TiO<sub>2</sub>, suggesting that STAO anchoring induces a chemical change from Ti<sup>4+</sup>-O to Ti<sup>3+</sup>-O in local environmental coordination. Figure S3a also verifies anchored TiO<sub>2</sub> leads to the formation of Ti<sup>3+</sup>, consistent with literatures elsewhere [34-36, 64-69]. The density of Ti<sup>3+</sup> would be boosted when raising the STAO density as shown

in Fig. S3b. To be specific, the densities of  $\text{Ti}^{3+}$  are increasing from 0.76% to 9.5%, corresponding to 0% to 8%-coverage STA0 (Fig. S3c-d). In addition, Fig. S3f shows that the peak at 533.5 eV is ascribed to the  $2p_{1/2}$  orbital of O in the  $\text{W}^{5+}$ -O bonds, and the peaks at 530 and 532.1 eV correspond to the  $2p_{1/2}$  and  $2p_{3/2}$  orbitals of O in  $\text{Ti}^{4+}$ -O and oxygen-vacancy (considered as  $\text{Ti}^{3+}$ -O), respectively. Compared with individual  $\text{Ti}^{3+}$ -O, there is no obvious valence change upon STA0 anchoring, further indicating that the STA0 sites are smoothly anchored on  $\text{TiO}_2$  surface as demonstrated in Fig. 1a.

Meanwhile, electron paramagnetic resonance (EPR) was applied to confirm the appearance of  $\text{Ti}^{3+}$ . Fig. 1g shows that a strong EPR peak is observed at a  $g$  value of 1.95, which can be ascribed to the unpaired electrons induced by surface oxygen-vacancy mediated  $\text{Ti}^{3+}$ . Moreover, as the STA0 anchoring density increases, the  $\text{Ti}^{3+}$ -O site EPR peak area also increases accordingly (Fig. S3e). Thus, EPR results further confirm that adatom at steps can induce  $\text{Ti}^{3+}$  formation, and the ratio between STA0 and  $\text{Ti}^{3+}$  density can be well controlled. Hence, in the following section,  $\text{Ti}^{3+}$ -dominant catalysts are used to describe the 0.1%-coverage STA0 catalysts, and the catalysts with 8%-coverage STA0 are regarded as  $\text{W}^{5+}$ -dominant catalysts and labelled as STA0/ $\text{TiO}_2$  for abbreviation.

To analyze the local environment of STA0 more thoroughly, the STA0/ $\text{TiO}_2$  are further examined by X-ray absorption near-edge structure (XANES) and extended X-ray absorption fine structure (EXAFS). Firstly, Fourier-Transformed (FT) EXAFS spectra (**Figure 2a**) shows one main peak at 1.6 Å of W-O in contrast to a W-W coordination peak at 2.6 Å shown in W foil, confirming the existence of single-atom W sites, consistent with HAADF and XRD (Figure S4). The patterns of various density STA0 (0.05, 0.5, 0.5, 1, 2 and 3 wt%)-anchored  $\text{TiO}_2$  are not different from that of pristine anatase- $\text{TiO}_2$ , suggesting the STA0 at step site has no periodic structure. However, when further increasing the amount of anchoring STA0, either a cluster or string structure (Figure S5) appears along Ti stripe, reaching a limitation with 8% coverage (3 wt%) of STA0. Moreover, the W-O bonding (1.6 Å) state of the atomically dispersed STA0 at  $\text{TiO}_2$  steps is different from the bonding state of the W-O bonds in  $\text{WO}_3$  (1.3 Å), suggesting that W-O bonds of STA0 at step sites are slightly distorted and stretched by surface Ti-O bonds. Additionally, the EXAFS fitting curve (Fig. 2c) confirms that the isolated W atom only coordinates with four oxygen atoms. As listed in **Table 1**, W-O bonds on STA0 site are grouped into two types: longer one of 2.19 Å and shorter one of 1.81 Å. The XANES spectra are analyzed on the absorption of W  $L_{III}$ -edge (Fig. 2b), where the white-line peak of STA0 is located between the  $\text{WO}_2$  and  $\text{WO}_3$ , revealing that the  $\text{W}^{5+}$  mainly presents. Combined with XPS results, the tetrahedron oxygen-coordinated  $\text{W}^{5+}$ - $\text{O}_4$  sites are anchored at steps as schematically shown in Fig. 2d.

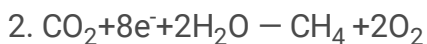
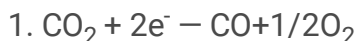
**Table 1** EXAFS fitting parameters at the W  $L_{III}$ -edge for various samples

Sample	Shell	$N^a$	$R(\text{\AA})^b$	$\sigma^2(\text{\AA}^2)^c$	$\Delta E_0(\text{eV})^d$	$R$ factor
STAO	W-O	3.3	1.81	0.0023	3.4	0.0041
	W-O	1.3	2.19	0.0023		
	W-O-Ti	1.9	3.45	0.0050		

<sup>a</sup> $N$ : coordination numbers; <sup>b</sup> $R$ : bond distance; <sup>c</sup> $\sigma^2$ : Debye-Waller factors; <sup>d</sup> $\Delta E_0$ : the inner potential correction.  $R$  factor: goodness of fit.  $S_0^2$  was set to 0.896, according to the experimental EXAFS fit of W foil by fixing CN as the known crystallographic value.

### Catalytic performance of STAO at TiO<sub>2</sub> atomic steps

Steps play a key role in catalysis, which could be further improved by anchoring STAO at the steps. A gas-solid interfacial CO<sub>2</sub> photoreduction was applied to evaluate the photocatalytic efficiency of the STAO-anchored anatase-TiO<sub>2</sub> photocatalysts. The photoreduction proceeded under mild conditions without any photosensitizer or sacrificial agents. **Figure 3** shows CO<sub>2</sub> conversion products as CH<sub>4</sub> (Fig. 3a) and CO (Fig. 3b) under the simulated sunlight irradiation for 5 h. These two main products are generated on distinct sites of W<sup>5+</sup>- and Ti<sup>3+</sup>-dominant catalysts, respectively. For W<sup>5+</sup>-dominant catalysts, it exhibits CH<sub>4</sub> generation with 59.3 mmol/g/h. Comparing with state-of-the-art catalysts without noble-metal in photocatalytic CO<sub>2</sub> reduction (Table S3), record-high efficiency is achieved by W<sup>5+</sup>-dominant TiO<sub>2</sub> photocatalysts, which exceeds those of pristine TiO<sub>2</sub> by more than one orders of magnitude. Notably, the selectivity is increased to 87.6% and 380 nm-induced apparent quantum yields on sites are 0.36 %, which is unprecedented in TiO<sub>2</sub> catalysts and comparative to the reported homogenous catalysts [39]. Meanwhile, for Ti<sup>3+</sup>-dominant catalysts, it can achieve 181.4  $\mu\text{mol g}^{-1} \text{h}^{-1}$  (87.8% electron selectivity) with CO as main product (CO-max). Besides, Fig. 3c further demonstrates that a growth in CH<sub>4</sub> production along with a decline in CO production occurs with increasing STAO densities, suggesting that the STAO sites result in the utilization of C<sub>1</sub> mass and electrons for CH<sub>4</sub> production. The CH<sub>4</sub> efficiency is highest one in TiO<sub>2</sub>-based photocatalysts without noble-metal. Furthermore, the relationship between the CH<sub>4</sub> product and STAO sites density is linear from 0.5-3 wt% as shown in Fig. 3c-3d. Therefore, through tuning the sites density, the photocatalysts can exhibit controllable two main products of CH<sub>4</sub> and CO, which are both important chemicals in practical industry. Additionally, 5-times cycling utilization was performed to demonstrate its remarkable stability as the photocatalysts with superior efficiency (Figure S6). To further illustrate its stability, the STAO at TiO<sub>2</sub> step sites after a long reaction were also examined by HAADF and XPS analyses (Figure S7). We also assessed reference samples without CO<sub>2</sub> gas and without H<sub>2</sub>O gas for comparison (Figure S8), showing that the CO<sub>2</sub> reduction and H<sub>2</sub>O splitting occur on the catalytic sites without any sensitizers or sacrifices. Although little extra surfactants are benefit for Ti<sup>3+</sup> appearance and might be involved in electron-hole separation [41, 83], the little residue of that has not much influence on CO or CH<sub>4</sub> reproductively generation in experiments.



## Mechanism of enhanced efficiency and selectivity by adatom at step sites

### (1) Photocarrier separation boosting catalytic efficiency

To illuminate the mechanism for the remarkably high efficiency of STAO at step sites, the photoelectric properties and kinetic pathway of photocarriers were systematically investigated. Photoluminescence (PL) quenching was conducted to reveal the separation of electron-hole pairs, as shown in **Figure 4a**. Significant quenching of PL is observed in catalysts with the STAO at step sites, indicating that the recombination of electron-hole pairs is effectively suppressed upon STAO anchoring. The electron-migration pathway is verified as transferring from  $\text{TiO}_2$  substrate to single-site due to the linear relationship between sites density and PL quenching degree as shown in inserted Fig. 4a. Furthermore, the photocurrent density with irradiation time increases as the density of STAO increases, further confirming the photoelectron separation and migration enhancement (Fig. 4b). Similarly, the charge migration improvement was also demonstrated by electrochemical impedance spectroscopy (EIS) analysis. Nyquist plots (Fig. 4c) show that the more STAO sites anchoring, the smaller of the impedance radii, indicating that the introduction of STAO sites greatly reduces the charge transfer resistance on catalysts.

A kinetic investigation of transient photoelectron's behavior on STAO sites was also accomplished. Transient fluorescence decay curves of various samples were collected (Figure S9). Analysis of the curves with re-convolution fitting manifests that the decays of each sample follows a bi-exponential model with  $t_1$  and  $t_2$  (Fig. 4d and Table S3). The pristine  $\text{TiO}_2$  exhibits a short lifetime of less than 200 ps due to the fast recombination of electron-hole. In contrast, "adatom at step" sites on  $\text{W}^{5+}$ -dominant catalysts demonstrates  $t_1=784$  ps and  $t_2=8576$  ps, especially the  $t_2$  enhancement from 31ps to 8576 ps is over 2 magnitudes, indicating the significant enhancement of electron-trapping on surface by  $\text{W}^{5+}$  sites. Even in the  $\text{Ti}^{3+}$ -dominant catalysts, the lifetime  $t_2$  can be extended to 3000 ps obviously. Thus, STAO at step sites lead to an increased trapped-electron lifetime and adjust it in a large degree. The  $t_2$  photoelectron lifetime (photoelectron on surface) is enhanced more obviously than that of  $t_1$  (photoelectron in deep band) as presented in Table S4. The noteworthy increased  $t_2$  lifetime via adatom at steps result from charge-transfer and charge-trapping at the surface sites, which could be beneficial for multi-electrons reactions. Besides, it is proven that further increasing STAO density (i.e. 4.5 wt%) would cause cluster formation, resulting in the decline of PL quenching (Figure S10). It indicates that STAO at step play a vital role on charge-transfer and charge-trapping, which might be related with unique electronic states of STAO [63].

## (2) CO<sub>2</sub>/CO adsorption-desorption and Gibbs free energy of intermediate

To reveal the mechanism of products selectivity in STAO at TiO<sub>2</sub> steps, the molecular adsorption-desorption was carried out, mainly considering CO and CO<sub>2</sub>. We calculated that the binding energy of CO<sub>2</sub> and CO adsorbed on Ti<sup>3+</sup>, Ti<sup>4+</sup> and W<sup>5+</sup> atom as shown in **Table 2**. For CO<sub>2</sub> adsorption, it indicates that W<sup>5+</sup> and Ti<sup>3+</sup> sites from STAO anchoring have stronger CO<sub>2</sub> binding energy than that of Ti<sup>4+</sup> site from pristine TiO<sub>2</sub>. The improved CO<sub>2</sub> adsorption on STAO at steps is further experimentally exhibited via temperature programmed desorption (Figure S11), which show that the amount of CO<sub>2</sub> adsorption molecule is distinctly increased on STAO at steps (W<sup>5+</sup> and Ti<sup>3+</sup>). Furthermore, via the in-situ diffuse reflectance infrared Fourier transform spectroscopy (DRIFTS), CO<sub>2</sub> and intermediates are vividly detected at the wavenumber from 1400-1800 cm<sup>-1</sup> (Figure 5a and Figure S12). For CO adsorption, W<sup>5+</sup> sites have stronger CO binding energy than other sites, which is also consistent with DRIFTS results, where CO adsorption signal is clearly observed in **Figure 5a**. It demonstrates absorbed CO can be observed at 2065 and 2080 cm<sup>-1</sup>, which decreases on Ti<sup>3+</sup> dominant catalysts and nearly absent on pristine TiO<sub>2</sub> (Ti<sup>4+</sup>). Gibbs free energy ( $\Delta G$ ) calculations were applied where all the presented intermediate states have been optimized after considering several most possibilities pathways with the lowest energies. (Figure S13a). Therefore, Ti<sup>3+</sup> and W<sup>5+</sup> sites are beneficial for CO production, and W<sup>5+</sup> sites are favorable for CH<sub>4</sub> production.

**Table 2.** Calculated adsorption energy of CO and CO<sub>2</sub> on W or Ti atom of STAO at TiO<sub>2</sub> step

	Ti <sup>3+</sup> -CO <sub>2</sub>	Ti <sup>3+</sup> -CO	W <sup>5+</sup> -CO <sub>2</sub>	W <sup>5+</sup> -CO	Ti <sup>4+</sup> -CO <sub>2</sub>	Ti <sup>4+</sup> -CO
E <sub>ad</sub> (eV)	-0.77	-0.96	-0.96	-1.41	-0.03	-0.85

To shed light on the mechanism of whole process of production of CH<sub>4</sub> from CO<sub>2</sub>, a STAO anchored at TiO<sub>2</sub> (145) step is established. The calculated  $\Delta G$  diagrams for CO<sub>2</sub> reduction into CH<sub>4</sub> and their relevant optimized structures are presented in Fig. 5b. Initially, CO<sub>2</sub> molecule energetically favors on W<sup>5+</sup> site (see table 2). When one H atom approaches to the adsorbed CO<sub>2</sub> molecule, it forms the usually reported OCOH\* [84] (step II). Then the intermediate OCOH\* nearly automatically dissociates to the adsorbed CO\* and OH\* (step III). Step by step, when one more H atom approaches to the adsorbed CO\* and OH\*, the formation of the first H<sub>2</sub>O molecule is more desirable, leaving the CO\* (step IV). The subsequent process is the CO reduction to CH<sub>4</sub>. One interesting phenomenon is the exchange of the adsorbed terminal point from C in OHC\* (step V) to O in OHHC\* (step VI). This process is quite important for the production of CH<sub>4</sub> because the exposed C atom could bind to maximum approaching H atoms readily. The intermediate

OHHHC\* (step VII) and O\* + CH<sub>4</sub> (step VIII) just correspond to more and more H atoms approaching to the exposed C atom, extremely facilitating to form the final production of CH<sub>4</sub>. As shown in Fig. 5b, the whole reaction from CO<sub>2</sub> to CH<sub>4</sub> is exothermic on STAO sites except for the formation of H<sub>2</sub>O, which possibly limiting the whole kinetics of CH<sub>4</sub> production. However, the endothermic feature from H<sub>2</sub>O formation can be easily overcome when involved with photons (step IX-X). Here, hole participation (simulating photon [85]) is intentionally involved, making the whole reaction process closed loop.

Interestingly, during the photocatalytic reduction reaction, rare amount of H<sub>2</sub> evolution is detected on W<sup>5+</sup>-dominant catalysts, indicating significant hydronation occurs on W<sup>5+</sup> sites. Moreover, Fig. 5a also show that the wavenumber at 1268, 1313, 2856 and 2900 cm<sup>-1</sup> ascribed as the stretching of C-H bonds increase from 10 to 60 mins, indicating C-H formation are gradually improved on the W<sup>5+</sup>-dominant sites. For Ti<sup>3+</sup>-dominant catalysts, as revealed in Figure S13b, CO hydronation on Ti<sup>3+</sup> has an uphill of 0.1 eV rather than -0.5 eV on W<sup>5+</sup> sites. Consistently, there is a ~1 eV barrier for the reaction from CO to CHO intermediate on Ti<sup>3+</sup> sites according to previous literatures [27, 29, 34], suggesting that CO desorption is more energy-favorable on Ti<sup>3+</sup>. Therefore, Ti<sup>3+</sup> sites are beneficial for CO<sub>2</sub> adsorption and CO releasing, while the specific sites of W<sup>5+</sup> kinetically accelerates the CH<sub>4</sub> production without releasing CO in the reaction process.

In photocatalytic CO<sub>2</sub> reduction, the photogenerated charges are produced based on semiconductor photo-electric effect. Band diagram of STAO at TiO<sub>2</sub> steps are explored to confirm that the CO<sub>2</sub> reduction on STAO at step sites is thermodynamically allowed. Figure S14a-d shows that both the band edges of high-density STAO anchored catalysts downshift to lower energy level compared with low-density STAO band structure. Such a shift is considered to be more favorable for CO<sub>2</sub> reduction. The STAO-induced interfacial band structure near the Fermi level ( $E_f$ ) was further verified by the flat band potentials determined by the Mott-Schottky plots obtained through EIS measurements (Fig. S14e). It is noted that STAO at step sites can tune the electrochemical redox potential, leaving the photoexcited electrons energy level are still within CO and CH<sub>4</sub> redox potentials. Additionally, Figure S15 shows surface area of the whole sites relatively decrease as W<sup>5+</sup> induction, indicating total amount of sites is not vital for the enhanced efficiency. The improved efficiency and products selectivity could be ascribed to the adatom sites where the introduction of STAO at steps yielding the formation of W<sup>5+</sup> and Ti<sup>3+</sup> sites, where have (1) enhanced electron-hole separations; (2) optimized molecular adsorption-desorption; (3) Gibbs free energy-favorable pathway.

In summary, for the first time, single-tungsten-atom-oxides were successfully anchored on steps of anatase-TiO<sub>2</sub> surface. The “adatom at step” sites achieve enhanced efficiency with selective products in

the CO<sub>2</sub> reduction reaction. Upon the rational design, main products of CH<sub>4</sub> and CO are realized on W<sup>5+</sup>-dominant catalysts and Ti<sup>3+</sup>-dominant catalysts, respectively. The ultrahigh CH<sub>4</sub> production efficiency with 59.3 mmol/g/h is attained in STA0/TiO<sub>2</sub> (8% coverage). This superior photocatalytic performance is resulted from the enhanced photocarrier separation and adsorption-desorption as well as satisfactory intermediates. This study elaborates the “adatom at step” is an effective strategy in photocatalysts design and provides a facile approach by anchoring single-sites at substrate steps. Such method could be extended to other catalytic sites to reach the optimized efficiency and excellent electron selectivity and provide an effective way to develop novel materials and eventually new physics and chemistry.

## Methods

**Materials.** Sodium tungstate dihydrate (Na<sub>2</sub>WO<sub>4</sub>·2H<sub>2</sub>O) were obtained from National Medicines Corporation Ltd. of China. Sulfuric acid (H<sub>2</sub>SO<sub>4</sub>), polyethylene glycol (molecular weight MW=200 Da, abbreviated as PEG-200), tetrabutyl titanate, ethanol and ethylene glycol (EG) were purchased from Aladdin chemical reagent Corp (Shanghai, China). All of which were of analytical grade and were used as received.

**Synthesis of anatase-TiO<sub>2</sub> nanoparticles.** Tetrabutyl titanate (30 ml) was transferred into a 50 ml Teflon-lined stainless-steel autoclave and heated at 180°C for 24 h. The resulting white precipitates were collected via centrifugation and further washed with ethanol and deionized water five times. They were subsequently dried in a vacuum oven at 80°C for 12 h, and the obtained anatase-TiO<sub>2</sub> nanoparticles were used for characterization and further preparation.

**Synthesis of the STA0-anchoring anatase-TiO<sub>2</sub> catalyst.** The synthesized method of STA0 precursor is modified upon our previous work [63]. Na<sub>2</sub>WO<sub>4</sub>·2H<sub>2</sub>O (2.27 mmol, 750 mg) and PEG-200 (1 ml) were dissolved in deionized water (10 ml), stirred for 30 min at ambient temperature, and then dilute sulfuric acid (20% H<sub>2</sub>SO<sub>4</sub>) was next added dropwise into the mixture until pH=5. The obtained solution was magnetically stirred in a light-free environment for 6 h, forming a transparent colorless solution for the next step. In a typical procedure for 3% STA0/TiO<sub>2</sub> synthesis, the as-synthesized TiO<sub>2</sub> powder (750 mg) was first dispersed in 30 ml of EG/H<sub>2</sub>O (1:10) mixture, and then 1200 µl of the as-synthesized STA0 was added to the suspension dropwise. The mixture was sealed, heated at 60°C for 2 h under vigorous stirring and then kept at room temperature for 12 h. Subsequently, the powder was heated in a 50 ml Teflon-lined stainless-steel autoclave at 180°C for 1 h. The final products were obtained by centrifugation and washed with ethanol and deionized water at least three times. Finally, they were dried at 60°C for 6 h in a vacuum oven before further characterization and catalysis testing. For 0.005% STA0, 0.05% STA0, 0.5% STA0, 1% STA0, 2% STA0 and 4.5% STA0 synthesis, a similar process to that used for 3% STA0

synthesis was followed, except that 5  $\mu\text{l}$ , 50  $\mu\text{l}$ , 200  $\mu\text{l}$ , 400  $\mu\text{l}$ , 800  $\mu\text{l}$  and 2500  $\mu\text{l}$  of STAO was added instead of 1200  $\mu\text{l}$  of STAO, respectively.

### **Photocatalytic CO<sub>2</sub> reduction condition**

The photocatalytic CO<sub>2</sub> reduction tests were performed in a multifunctional photochemical reactor (PLR MFPR-1, Beijing Perfectlight Corp.). Typically, 10 mg of photocatalyst powder was dispersed in 1 ml water by ultrasonic method, and was dripped on 2.5\*3.5 cm<sup>2</sup> glass slide. After natural drying, the photocatalyst was dried in 75 °C oven for 2 h, and then irradiated with 254 nm UV lamp for 2 h to remove the organic adsorbent on the catalyst surface. The reaction conditions were controlled at 40°C, 0.26MPa. 200  $\mu\text{l}$  deionized water was added into the reactor. A 300 W Xe lamp (Microsolar300, Beijing Perfectlight Corp.) with AM1.5 solar simulation filter was used as the light source. The optical density was measured to be 455 mWcm<sup>-2</sup> at the reaction position. The gas evolutions were analysed by gas chromatography (GC-2002, Shanghai Kechuang Corp.).

**Photocatalyst characterization.** HR-TEM, scanning transmission electron microscopy (STEM)-HAADF and energy-dispersive X-ray spectroscopy (EDX) elemental mapping characterization was performed by a Titan Themis G2 transmission electron microscope operated at 300 kV and equipped with a probe spherical aberration corrector. XRD data were acquired via a Bruker D8-Advance X-ray powder diffractometer with Cu K $\alpha$  radiation ( $\lambda=1.5406 \text{ \AA}$ ). ICP-OES measurements were conducted on an Agilent ICP-OES-730 analyser. The binding energies obtained in the XPS spectral analysis were corrected for specimen charging by referencing C 1s to 284.8 eV. The ESR spectra were measured on Bruker A300-10/12 ESR spectrometer. UV–Vis spectra were acquired with a Hitachi U-3900 UV–Vis spectrophotometer. PL spectroscopy was performed on a Hitachi F-7000 fluorescence spectrometer with an excitation wavelength of 290 nm. The electrochemical measurements were performed in a conventional three-electrode cell on a CHI-760E electrochemical workstation (Shanghai Chenhua Instrument Co., Ltd, China). During the photocurrent measurement, an Ag/AgCl electrode was used as the reference electrode and a Pt nanosheets electrode acted as the counter electrode. The working electrodes were designed using resulting samples covered on the surface of fluoride tin oxide (FTO) conductor glass. A quartz cell filled with 0.5 M Na<sub>2</sub>SO<sub>4</sub> (pH = 6.8) electrolyte was used as the measure system. For electrochemical impedance spectroscopy (EIS) measurements, the amplitude of the sinusoidal wave was 5 mV, and the frequency range from 100 kHz to 0.1 Hz. The W L<sub>III</sub>-edge X-ray absorption fine structure (XAFS) spectra of the sample and standards were collected at the beamline BL14W1 of the Shanghai Synchrotron Radiation Facility (SSRF). The white light was monochromatized by a Si (111) double-crystal monochromator and calibrated with W foil. The XAFS spectra of sample and standards were recorded in fluorescence and transmission mode, respectively.

## Computational details

All the Spin-polarized first-principles density functional theory (DFT) calculations were performed using the Perdew-Burke-Ernzerhof (PBE) functional [86] as implemented in the Vienna ab initio Simulation Package [87, 88]. The projector augmented-wave method [89] was used to treat the ion-electron interactions. The cutoff energy of the plane-wave basis was set to 400 eV and a  $2\times 3\times 1$  k-point mesh was used for Brillouin zone integration. The internal structures were fully relaxed until the Hellman-Feynman forces on all atoms were less than  $0.02 \text{ eV \AA}^{-1}$ . Dipole moment corrected was made accordingly in the  $z$  direction, and the empirical correction scheme of Grimme [90] was also performed, where the effect of vdW interactions was included explicitly. We construct a  $(2\times 1)$  supercell slabs including five atomic layers for the anatase  $\text{TiO}_2$  stepped surfaces [75]. A vacuum of more than  $15 \text{ \AA}$  was used to avoid the interaction between slabs. The  $\text{TiO}_2$  (101) surface terminates with two types of Ti cation, five-fold coordinated Ti and six-fold coordinated Ti, and two types of O anion, two-fold coordinated O sites and three-fold coordinated O sites. The Gibbs free energies of the  $\text{CO}_2$  Reduction were computed from  $\Delta G = \Delta E_{\text{DFT}} + \Delta E_{\text{ZPE}} - T\Delta S$ , where the total energy change ( $\Delta E_{\text{DFT}}$ ), zero-point energy change ( $\Delta E_{\text{ZPE}}$ ), and the entropy change ( $\Delta S$ ) of each adsorbed state were calculated according to the standard molar Gibbs energy of formation at 298.15 K.

## Declarations

### Acknowledgements

This work was supported by the Natural Science Foundation of China (NSFC) (Grant No. 91860202, 51988101, 11404014, 51471008, 11327901, 11974088, 51872008, and 41701359, “111” project under the grant of DB18015, Natural Science Foundation of Beijing Municipality (Z180014, 2192008) and Beijing Outstanding Young Scientists Projects BJJWZYJH01201910005018. X. Zhou acknowledges financial support from NSFC Grant No. 11674040, 11904039 and the Fundamental Research Funds for the Central Universities (106112017CDJQJ308821). We thank Mr. X. J. Chen, Dr. D. L. Kong, Y. Z. Guo, L. B. Fu, X. L. Qu, Prof. Z. G. Yan, Dr. J. W. Xiao and T. F. Lin for providing measurement support, and we also thank Prof. Y. Yu and Prof. Z. X. Li for discussions. We also gratefully acknowledge the staff of beamline BL14W1 at Shanghai Synchrotron Radiation Facility for their support in XAFS measurements.

## References

1. Panwar, N. L., Kaushik, S. C. & Kothari, S. Role of renewable energy sources in environmental protection: A review. *Renew. Sustain. Energy Rev.* **15**, 1513-1524 (2011).
2. Chu, S., Cui, Y. & Liu, N. The path towards sustainable energy. *Nat. Mater.* **16**, 16-22 (2017).
3. Vogt, C., Monai, M., Kramer, G. J. & Weckhuysen, B. M. The renaissance of the Sabatier reaction and its applications on Earth and in space. *Nat. Catal.* **2**, 188-197 (2019).

4. Zhang, S., Fan, Q., Xia, R. & Meyer, T. J. CO<sub>2</sub> reduction: from homogeneous to heterogeneous electrocatalysis. *Acc. Chem. Res.* **53**, 255-264 (2020).
5. Qiao, J. L., Liu, Y. Y., Hong, F. & Zhang, J. J. A review of catalysts for the electroreduction of carbon dioxide to produce low-carbon fuels. *Chem. Soc. Rev.*, **43**, 631-675 (2014).
6. Wang, W. H., Himeda, Y., Muckerman, J. T., Manbeck, G. F. & Fujita, E. CO<sub>2</sub> hydrogenation to formate and methanol as an alternative to photo- and electrochemical CO<sub>2</sub> Reduction. *Chem. Rev.* **115**, 12936-12973 (2015).
7. Ran, J. R., Jaroniec, M. & Qiao, S. Z. Cocatalysts in semiconductor-based photocatalytic CO<sub>2</sub> reduction: achievements, challenges, and opportunities. *Adv. Mater.* **30**, 1704649 (2018).
8. Chang, X. X., Wang, T. & Gong, J. L. CO<sub>2</sub> photo-reduction: insights into CO<sub>2</sub> activation and reaction on surfaces of photocatalysts. *Energy Environ. Sci.* **9**, 2177-2196 (2016).
9. Chen, G. B. et al. Solar-to-fuels: recent advances in light-driven C1 chemistry. *Angew. Chem. Int. Ed.* **58**, 17528-17551 (2019).
10. Li, X., Yu, J., Wageh, S., Alghamdi, A. A. & Xie, J. Graphene in photocatalysis: a review. *Small* **12**, 6640-6696 (2016).
11. Tu, W. G., Zhou, Y. & Zou, Z. G. Photocatalytic conversion of CO<sub>2</sub> into renewable hydrocarbon fuels: state-of-the-art accomplishment, challenges, and prospects. *Adv. Mater.* **26**, 4607-4626 (2014).
12. Pan, Y. et al. Design of Single-Atom Co-N<sub>5</sub> Catalytic Site: A Robust Electrocatalyst for CO<sub>2</sub> Reduction with Nearly 100% CO Selectivity and Remarkable Stability. *J. Am. Chem. Soc.* **140**, 4218-4221 (2018).
13. Cao, S. F. et al. Single-atom gold oxo-clusters prepared in alkaline solutions catalyse the heterogeneous methanol self-coupling reactions. *Nat. Chem.* **11**, 1098-1105 (2019).
14. Yang, H. B. et al. Atomically dispersed Ni(I) as the active site for electrochemical CO<sub>2</sub> reduction. *Nat. Energy* **3**, 140-147 (2018).
15. Dong, C. Y., et al. Size-dependent activity and selectivity of carbon dioxide photocatalytic reduction over platinum nanoparticle. *Nat. Commun.* **9**, 1252 (2018).
16. Kong, T. T., Jiang, Y. W., Xiong, Y. J. Photocatalytic CO<sub>2</sub> conversion: what can we learn from conventional CO<sub>x</sub> hydrogenation. *Chem. Soc. Rev.* **49**, 6579-6591 (2020).
17. Yang, D., et al. Visible-light-switched electron transfer over single porphyrin-metal atom center for highly selective electroreduction of carbon dioxide. *Nat. Commun.* **10**, 3844 (2019).
18. Chen, Y. Z., et al. Optimizing reaction paths for methanol synthesis from CO<sub>2</sub> hydrogenation via metal-ligand cooperativity. *Nat. Commun.* **10**, 1885 (2019).
19. Dinh, C.-T. et al. CO<sub>2</sub> electroreduction to ethylene via hydroxide-mediated copper catalysis at an abrupt interface. *Science* **360**, 783-787 (2018).
20. Huang, H. et al. Solar-light-driven CO<sub>2</sub> reduction by CH<sub>4</sub> on silica-cluster-modified Ni nanocrystals with a high solar-to-fuel efficiency and excellent durability. *Adv. Energy Mater.* **8**, 1702472 (2018).

21. Iwase, A. et al. Water splitting and CO<sub>2</sub> reduction under visible light irradiation using Z-scheme systems consisting of metal sulfides, CoO<sub>x</sub>-loaded BiVO<sub>4</sub>, and a reduced graphene oxide electron mediator. *J. Am. Chem. Soc.* **138**, 10260–10264 (2016).
22. Cao, S. W. et al. 2D/2D heterojunction of ultrathin MXene/Bi<sub>2</sub>WO<sub>6</sub> nanosheets for improved photocatalytic CO<sub>2</sub> reduction. *Adv. Funct. Mater.* **28**, 1800136 (2018).
23. Jiang, Z. F. et al. A hierarchical Z-scheme α-Fe<sub>2</sub>O<sub>3</sub>/g-C<sub>3</sub>N<sub>4</sub> hybrid for enhanced photocatalytic CO<sub>2</sub> reduction. *Adv. Mater.* **30**, 1706108 (2018).
24. Haviv, E., Shimon, L. J. W. & Neumann, R. Photochemical reduction of CO<sub>2</sub> with visible light using a polyoxometalate as photoreductant. *Chem. Eur. J.* **23**, 92-95 (2017).
25. Schreier, M. et al. Solar conversion of CO<sub>2</sub> to CO using Earth-abundant electrocatalysts prepared by atomic layer modification of CuO. *Nat. Energy* **2**, 17087 (2017).
26. Ji, Y. F. & Luo, Y. New mechanism for photocatalytic reduction of CO<sub>2</sub> on the anatase TiO<sub>2</sub> (101) surface: the essential role of oxygen vacancy. *J. Am. Chem. Soc.* **138**, 15896-15902 (2016).
27. Liu, J. Y., Gong, X. Q. & Alexandrova, A. N. Mechanism of CO<sub>2</sub> photocatalytic reduction to methane and methanol on defected anatase TiO<sub>2</sub> (101): a density functional theory study. *J. Phys. Chem. C.* **123**, 3505-3511 (2019).
28. Wang, S. L. et al. Porous hypercrosslinked polymer-TiO<sub>2</sub>-graphene composite photocatalysts for visible-light-driven CO<sub>2</sub> conversion. *Nat. Commun.* **10**, 676 (2019).
29. Yin, G. H. et al. Hydrogenated blue titania for efficient solar to chemical conversions: preparation, characterization, and reaction mechanism of CO<sub>2</sub> reduction. *ACS Catal.* **8**, 1009-1017 (2018).
30. Collado, L., et al. Unravelling the effect of charge dynamics at the plasmonic metal/semiconductor interface for CO<sub>2</sub> photoreduction. *Nat. Commun.* **9**, 4986 (2018).
31. Zhang, L. Y., Can, M., Ragsdale, S.W. & Armstrong, F. A. Fast and selective photoreduction of CO<sub>2</sub> to CO catalyzed by a complex of carbon monoxide dehydrogenase, TiO<sub>2</sub>, and Ag nanoclusters. *ACS Catal.* **8**, 2789-2795 (2018).
32. Yu, J. G., Low, J. X., Xiao, W., Zhou, P. & Jaroniec, M. Enhanced photocatalytic CO<sub>2</sub>-reduction activity of anatase TiO<sub>2</sub> by coexposed {001} and {101} facets. *J. Am. Chem. Soc.* **136**, 8839-8842 (2014).
33. Xing, M. Y. et al. Modulation of the Reduction Potential of TiO<sub>2-x</sub> by Fluorination for Efficient and Selective CH<sub>4</sub> Generation from CO<sub>2</sub> Photoreduction. *Nano Lett.* **18**, 3384-3390 (2018).
34. Liu, G. et al. A red anatase TiO<sub>2</sub> photocatalyst for solar energy conversion. *Energy Environ. Sci.* **5**, 9603-9610 (2012).
35. Zou, Z. G., Ye, J. H., Sayama, K. & Arakawa, H. Direct splitting of water under visible light irradiation with an oxide semiconductor photocatalyst. *Nature* **414**, 625-627 (2001).
36. Yu, J.G., Qi, L. F. & Jaroniec, M. Hydrogen production by photocatalytic water splitting over Pt/TiO<sub>2</sub> nanosheets with exposed (001) facets. *J. Phys. Chem. C* **114**, 13118-13125 (2010).

37. Rao, H., Schmidt, L. C., Bonin, J. & Robert, M. Visible-light-driven methane formation from CO<sub>2</sub> with a molecular iron catalyst. *Nature* **548**, 74-77 (2017) .
38. Takeda, H., Ohashi, K., Sekine, A. & Ishitani, O. Photocatalytic CO<sub>2</sub> reduction using Cu(I) photosensitizers with a Fe(II) catalyst. *J. Am. Chem. Soc.* **138**, 4354-4357 (2016).
39. Elgrishi, N., Chambers, M. B., Wang, X. & Fontecave, M. Molecular polypyridine-based metal complexes as catalysts for the reduction of CO<sub>2</sub>. *Chem. Soc. Rev.* **46**, 761-796 (2017).
40. Kuriki, R. et al. Nature-inspired, highly durable CO<sub>2</sub> reduction system consisting of a binuclear ruthenium (II) complex and an organic semiconductor using visible light. *J. Am. Chem. Soc.* **138**, 5159-5170 (2016).
41. Gu, J., Hsu, C.-S., Bai, L. C., Chen, H. M. & Hu, X. L. Atomically dispersed Fe<sup>3+</sup> sites catalyze efficient CO<sub>2</sub> electroreduction to CO. *Science* **364**, 1091-1094 (2019).
42. Jiang, Z. et al. Filling metal-organic framework mesopores with TiO<sub>2</sub> for CO<sub>2</sub> photoreduction. *Nature* 1-8 (2020).
43. Logan, M. W. et al. Systematic variation of the optical bandgap in titanium based iso-reticular metal-organic frameworks for photocatalytic reduction of CO<sub>2</sub> under blue light. *J. Mater. Chem. A* **5**, 11854-11863 (2017)
44. Li, R. et al. Integration of an inorganic semiconductor with a metal-organic framework: a platform for enhanced gaseous photocatalytic reactions. *Adv. Mater.* **26**, 4783-4788 (2014).
45. Crake, A., Angus C., Christoforidis, K. C., Kafizas, A., Zafeiratos, S. & Petit, C. CO<sub>2</sub> capture and photocatalytic reduction using bifunctional TiO<sub>2</sub>/MOF nanocomposites under UV-vis irradiation. *Appl. Catal. B: Environ.* **210**, 131-140 (2017).
46. Lin, S. et al. Covalent organic frameworks comprising cobalt porphyrins for catalytic CO<sub>2</sub> reduction in water. *Science* **349**, 1208-1213 (2015).
47. Zhang, H. B. et al. Efficient visible-light-driven carbon dioxide reduction by a single-atom implanted metal-organic framework. *Angew. Chem. Int. Ed.* **128**, 14310-14314 (2016).
48. Ju, W., et al. Unraveling mechanistic reaction pathways of the electrochemical CO<sub>2</sub> reduction on Fe-N-C single-site catalysts. *ACS Energy Lett.* **4**, 1663-1671 (2019).
49. Zhang, E. H. .et al. Bismuth single atoms resulting from transformation of metal-organic frameworks and their use as electrocatalysts for CO<sub>2</sub> reduction. *J. Am. Chem. Soc.* **141**, 16569-16573 (2019).
50. Weng, Z. et al. Active sites of copper-complex catalytic materials for electrochemical carbon dioxide reduction. *Nat. Commun.* **9**, 415 (2018).
51. Liu, S. et al. Identifying active sites of nitrogen-doped carbon materials for the CO<sub>2</sub> reduction reaction. *Adv. Funct. Mater.* **28**, 1800499 (2018).
52. Su, X., Yang, X. F., Huang, Y. Q., Liu, B. & Zhang, T. Single-atom catalysis toward efficient CO<sub>2</sub> Conversion to CO and formate products. *Acc. Chem. Res.* **52**, 656-664 (2019).

53. Wan, J. W. et al. Defect effects on TiO<sub>2</sub> nanosheets: stabilizing single atomic site Au and promoting catalytic properties. *Adv. Mater.* **30**, 1705369 (2018).
54. Matsubu, J. C. et al. Adsorbate-mediated strong metal-support interactions in oxide-supported Rh catalysts. *Nat. Chem.* **9**, 120-127 (2017).
55. Wang, Y. F. et al. Single-atomic Cu with multiple oxygen vacancies on ceria for electrocatalytic CO<sub>2</sub> reduction to CH<sub>4</sub>. *ACS Catal.* **8**, 7113-7119 (2018).
56. Li, X. D. et al. Selective visible-light-driven photocatalytic CO<sub>2</sub> reduction to CH<sub>4</sub> mediated by atomically thin CuIn<sub>5</sub>S<sub>8</sub> layers. *Nat. Energy* **4**, 690-699 (2019).
57. Gao, C. et al, Heterogeneous single-atom catalyst for visible-light driven high-turnover CO<sub>2</sub> reduction: the role of electron transfer. *Adv. Mater.* **30**, 1704624 (2018).
58. Zhang, H.B, et al. Efficient visible-light-driven carbon dioxide reduction by a single-atom implanted metal-organic framework. *Angew. Chem.* **128**, 14522-14526 (2016).
59. Xu Y. F. et al. A CsPbBr<sub>3</sub> perovskite quantum dot/graphene oxide composite for photocatalytic CO<sub>2</sub> reduction. *J. Am. Chem. Soc.* **139**, 5660-5663 (2017).
60. Zhang, H. B, et al. Surface-plasmon-enhanced photodriven CO<sub>2</sub> reduction catalyzed by metal-organic-framework-derived iron nanoparticles encapsulated by ultrathin carbon layers. *Adv. Mater.* **28**, 3703-3710 (2018).
61. Gao, S. et al. Highly efficient and exceptionally durable CO<sub>2</sub> photoreduction to methanol over freestanding defective single-unit-cell bismuth vanadate layers. *J. Am. Chem. Soc.* **139**, 3438-3445 (2017).
62. Liang, L. et al. Single unit cell bismuth tungstate layers realizing robust solar CO<sub>2</sub> reduction to methanol. *Angew. Chem. Int. Ed.* **54**, 13971-13974 (2015).
63. Wang, C. et al. Ultrahigh photocatalytic rate at a single-metal-atom-oxide. *Adv. Mater.* **31**, 1903491 (2019).
64. Hejazi, S. et al. On the controlled loading of single platinum atoms as a co-catalyst on TiO<sub>2</sub> anatase for optimized photocatalytic H<sub>2</sub> generation. *Adv. Mater.* 1908505 (2020).
65. Hoang, S. et al. Activating low-temperature diesel oxidation by single-atom Pt on TiO<sub>2</sub> nanowire array. *Nat. Commun.* **11**, 1062 (2020).
66. Tang, Y. et al. Rh single atoms on TiO<sub>2</sub> dynamically respond to reaction conditions by adapting their site. *Nat. Commun.* **9**, 4488 (2019).
67. Zhang, Z., Tang, W. J., Neurock, M. & Yates, J. T. Electric Charge of Single Au Atoms Adsorbed on TiO<sub>2</sub> (110) and Associated Band Bending. *J. Phys. Chem. C* **115**, 23848-23853 (2011).
68. Gao, G. P., Jiao, Y., Waclawik, E.R. & Du, A.J. Single atom (Pd/Pt) supported on graphitic carbon nitride as an efficient photocatalyst for visible-light reduction of carbon dioxide. *J. Am. Chem. Soc.* **138**, 6292-6297 (2016).

69. DeRita, L. et al. Catalyst architecture for stable single atom dispersion enables site-specific spectroscopic and reactivity measurements of CO adsorbed to Pt atoms, oxidized Pt clusters, and metallic Pt clusters on TiO<sub>2</sub>. *J. Am. Chem. Soc.* **139**, 14150-14165 (2017).
70. Iyemperumal, S. K., Pham, T. D., Bauer, J. & Deskins, N. A. Quantifying support interactions and reactivity trends of single metal atom catalysts over TiO<sub>2</sub>. *J. Phys. Chem. C* **122**, 25274-25289 (2018).
71. Yi, L. H., Lan, F. J., Li J. G. & Zhao, C. X. Efficient noble-metal-free Co-NG/TiO<sub>2</sub> photocatalyst for H<sub>2</sub> evolution: synergistic effect between single-atom Co and N-Doped graphene for enhanced photocatalytic activity. *ACS Sustain. Chem. Eng.* **6**, 12766-12775 (2018).
72. Chen, J. B. et al. Synergy between defects, photoexcited electrons, and supported single atom catalysts for CO<sub>2</sub> reduction. *ACS Catal.* **8**, 10464-10478 (2018).
73. Matsubu, J. C., Yang, V. N. & Christopher, P. Isolated metal active site concentration and stability control catalytic CO<sub>2</sub> reduction selectivity. *J. Am. Chem. Soc.* **137**, 3076-3084 (2015).
74. Lee, B. H. et al. Reversible and cooperative photoactivation of single-atom Cu/TiO<sub>2</sub> photocatalysts. *Nat. Mater.* **18**, 620-626 (2019).
75. Derita, L. et al. Structural evolution of atomically dispersed Pt catalysts dictates reactivity. *Mater.* **18**, 746-751 (2019).
76. Mino, L., Spoto, G. & Ferrari, A. M. CO<sub>2</sub> capture by TiO<sub>2</sub> anatase surfaces: a combined DFT and FTIR study. *J. Phys. Chem. C* **118**, 25016-25026 (2014).
77. Setvin, M. et al. Charge trapping at the step edges of TiO<sub>2</sub> anatase (101). *Angew. Chem. Int. Ed.* **53**, 4714-4716 (2014)
78. Gong, X. Q. & Selloni, A. Role of steps in the reactivity of the anatase TiO<sub>2</sub>(101) surface. *J. Catal.* **249**, 134-139 (2007).
79. Thompson, T. L. & Yates, J. T. Surface science studies of the photoactivation of TiO<sub>2</sub>-new photochemical processes. *Chem. Rev.* **106**, 4428-4453 (2006).
80. Thang, H. V. & Pacchioni, G. Nature of atomically dispersed Ru on anatase TiO<sub>2</sub>: revisiting old data based on DFT calculations. *J. Phys. Chem. C* **123**, 7271-7282 (2019).
81. Gong, X. Q., Selloni, A. Batzill, M. & Diebold, U. Steps on anatase TiO<sub>2</sub> (101). *Nat. Mater.* **5** 665-670 (2006).
82. Diebold, U. The surface science of titanium dioxide. *Surf. Sci. Rep.* **48**, 53-229 (2003)
83. Nam, D. H. et al. Molecular enhancement of heterogeneous CO<sub>2</sub> reduction. *Nat. Mater.*, **19**, 266-276 (2020).
84. Wu, X., et al. Photocatalytic CO<sub>2</sub> conversion of M<sub>0.33</sub>WO<sub>3</sub> directly from the air with high selectivity: insight into full spectrum-induced reaction mechanism. *J. Am. Chem. Soc.* **141**, 5267-5274 (2019).
85. Lucking, M. et al. A nucleus-coupled electron transfer mechanism for TiO<sub>2</sub>-catalyzed water splitting. *Phys. Chem. Chem. Phys.* **17**, 16779 (2015).

86. Perdew, J. P., Burke, K., Ernzerhof, M. *Phys. Rev. Lett.* **77**, 3865 (1996).
87. Kresse, G., Hafner, J., *Phys. Rev. B* **47** 558 (1993).
88. Kresse, G., Furthmüller, J., *Phys. Rev. B* **54** 11169 (1996).
89. Blöchl, P. E., *Phys. Rev. B* **50** 17953 (1994).
90. Grimme, S., *J. Comput. Chem.* **27**, 1787 (2006).

## Figures

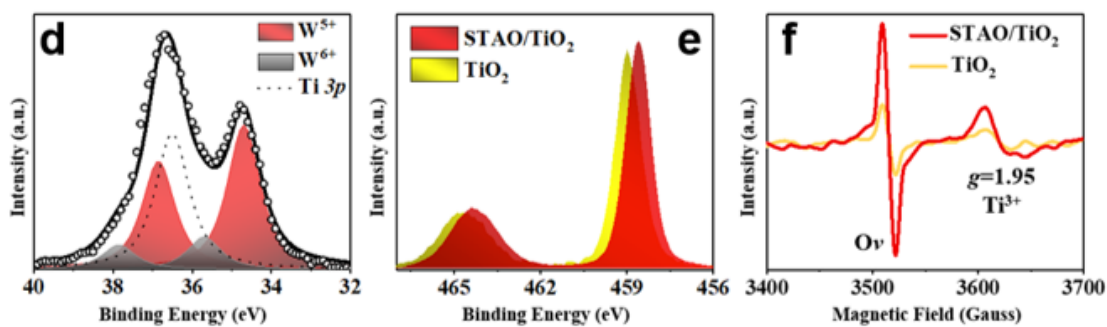
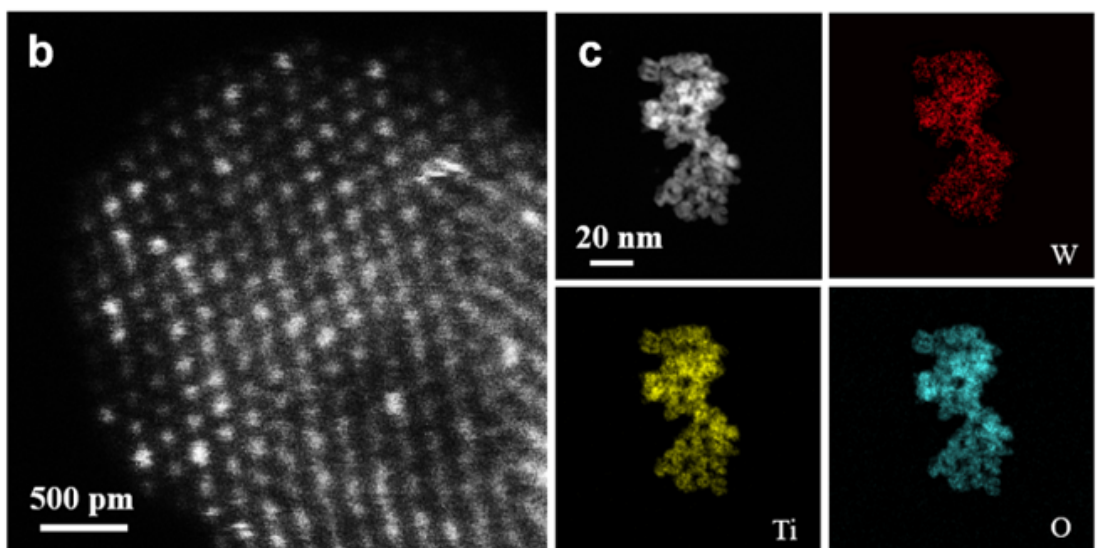
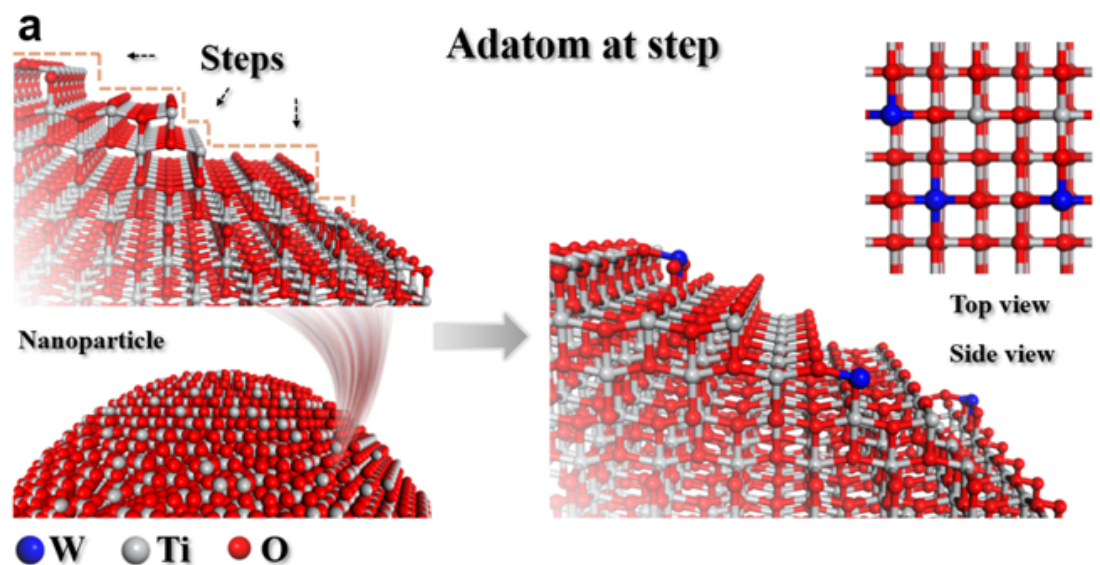


**Figure 1**

Characterization of STA0 at anatase-TiO<sub>2</sub> atomic step. a Schematically anchored STA0 at TiO<sub>2</sub> atomic step. b, HAADF image of STA0/TiO<sub>2</sub> showing the atomic location of tungsten (bright spots) on titanium atoms column (grey spots). c, Elemental mapping analysis of STA0/TiO<sub>2</sub>; scale bar 20 nm. d, XPS spectra of W and. e, Ti elements on STA0/TiO<sub>2</sub>. f, Electron paramagnetic resonance spectra of catalysts before and after STA0 anchoring.

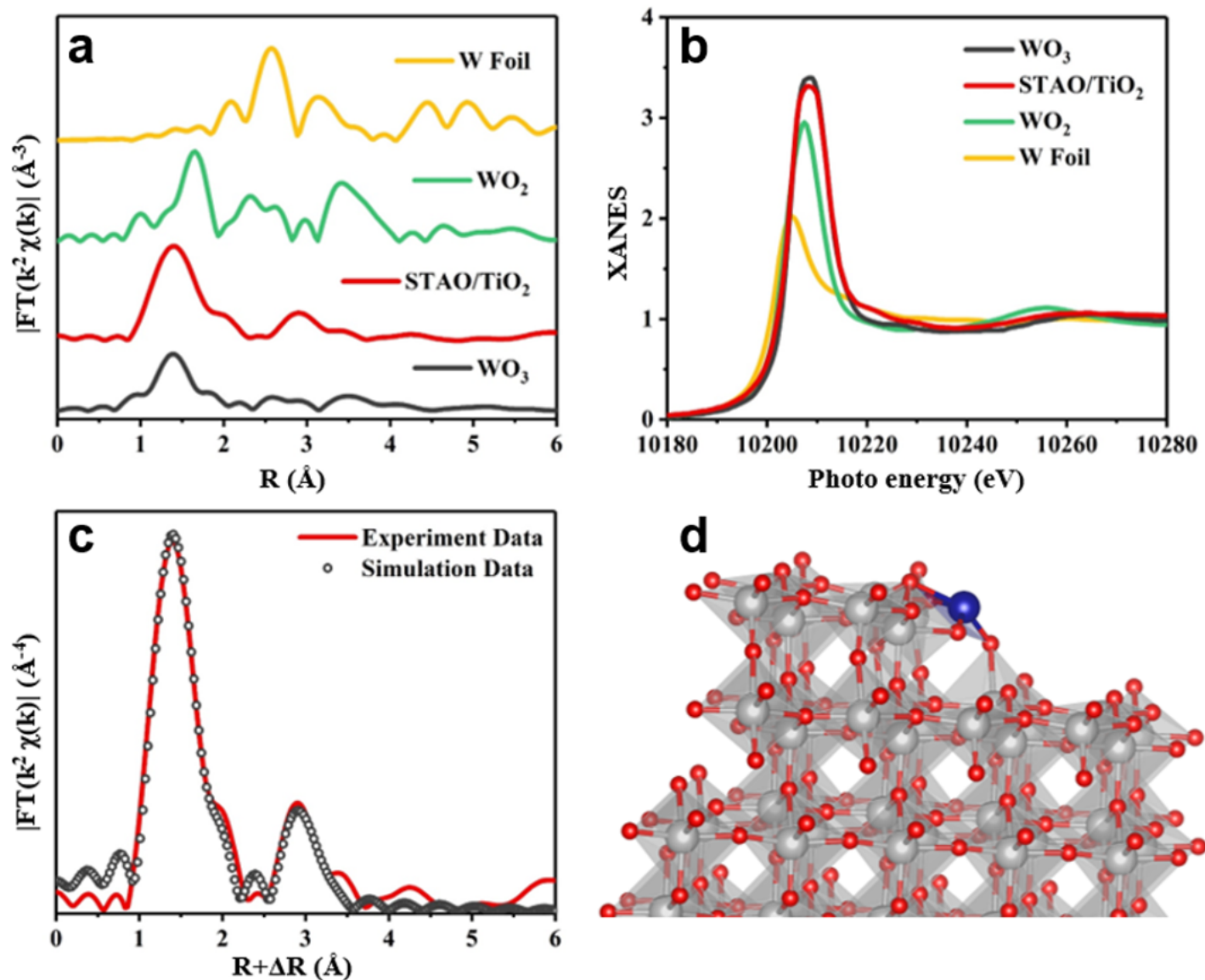


**Figure 2**

Local environmental coordination of STAO at TiO<sub>2</sub> atomic step. a, The corresponding K<sub>2</sub>-weighted FT spectra of STAO/TiO<sub>2</sub>, WO<sub>2</sub>, WO<sub>3</sub> and W foil, the last three materials were used as reference samples. b, The W L<sub>III</sub>-edge XANES spectra. c, Comparison of FT-EXAFS curves between the experimental data and the fitted spectra of STAO/TiO<sub>2</sub>. d, Schematically 4-oxygen coordinated tungsten atom units at TiO<sub>2</sub> steps model.

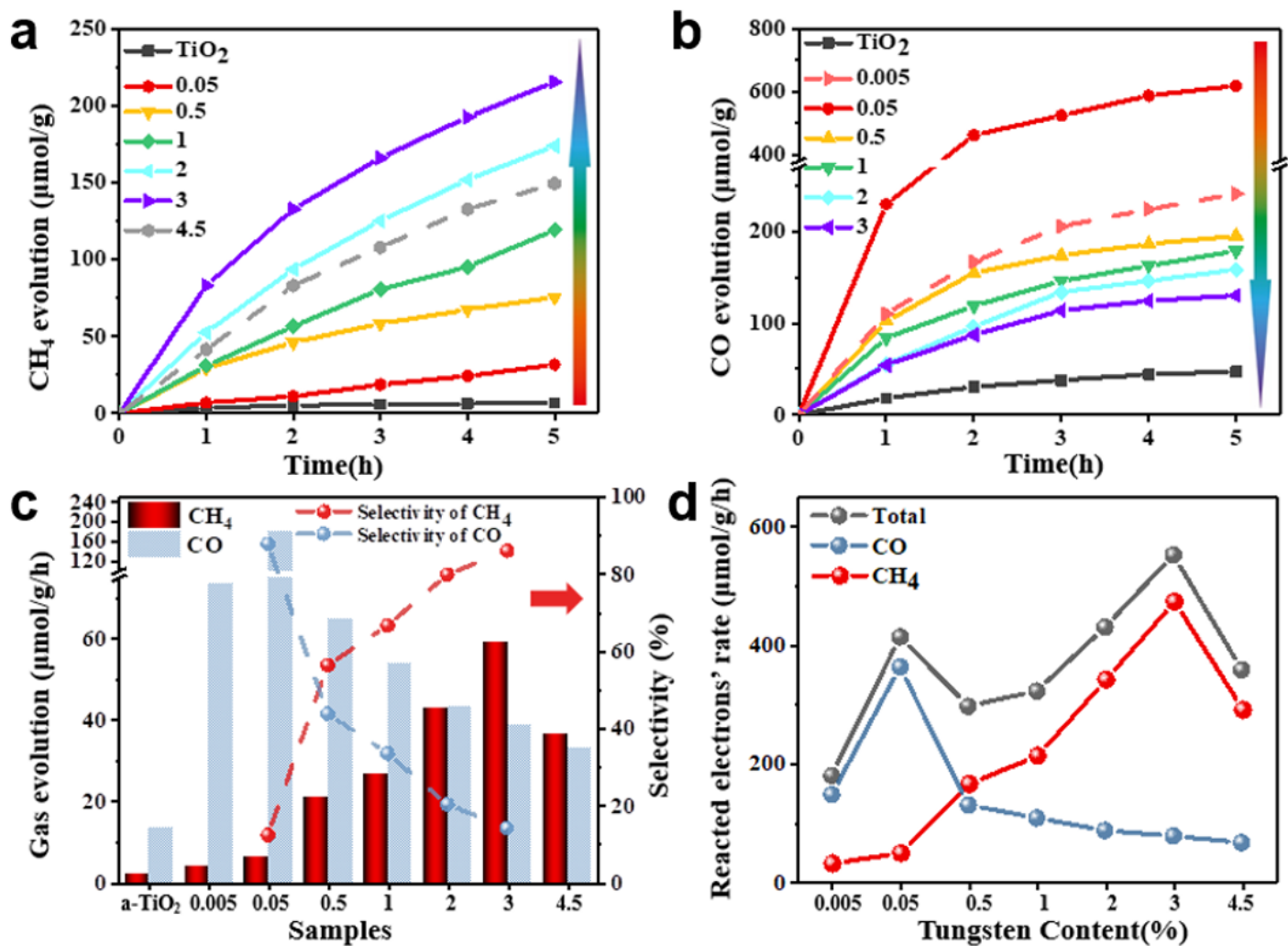


**Figure 3**

Catalytic performance of STA0 anchored catalysts in the CO<sub>2</sub> reduction reaction. Time-dependent production of a CH<sub>4</sub> and b CO evolution in photocatalytic CO<sub>2</sub> reduction by catalysts with various STA0 density. c, Average photocatalytic efficiency of catalysts with different STA0 sites density during 12 h of irradiation. The dashed line in the inset is the electron selectivity of CH<sub>4</sub> and CO in the various catalysts. d, Electron reacted utilization rate of total, CO and CH<sub>4</sub> along with the increase of anchored STA0.

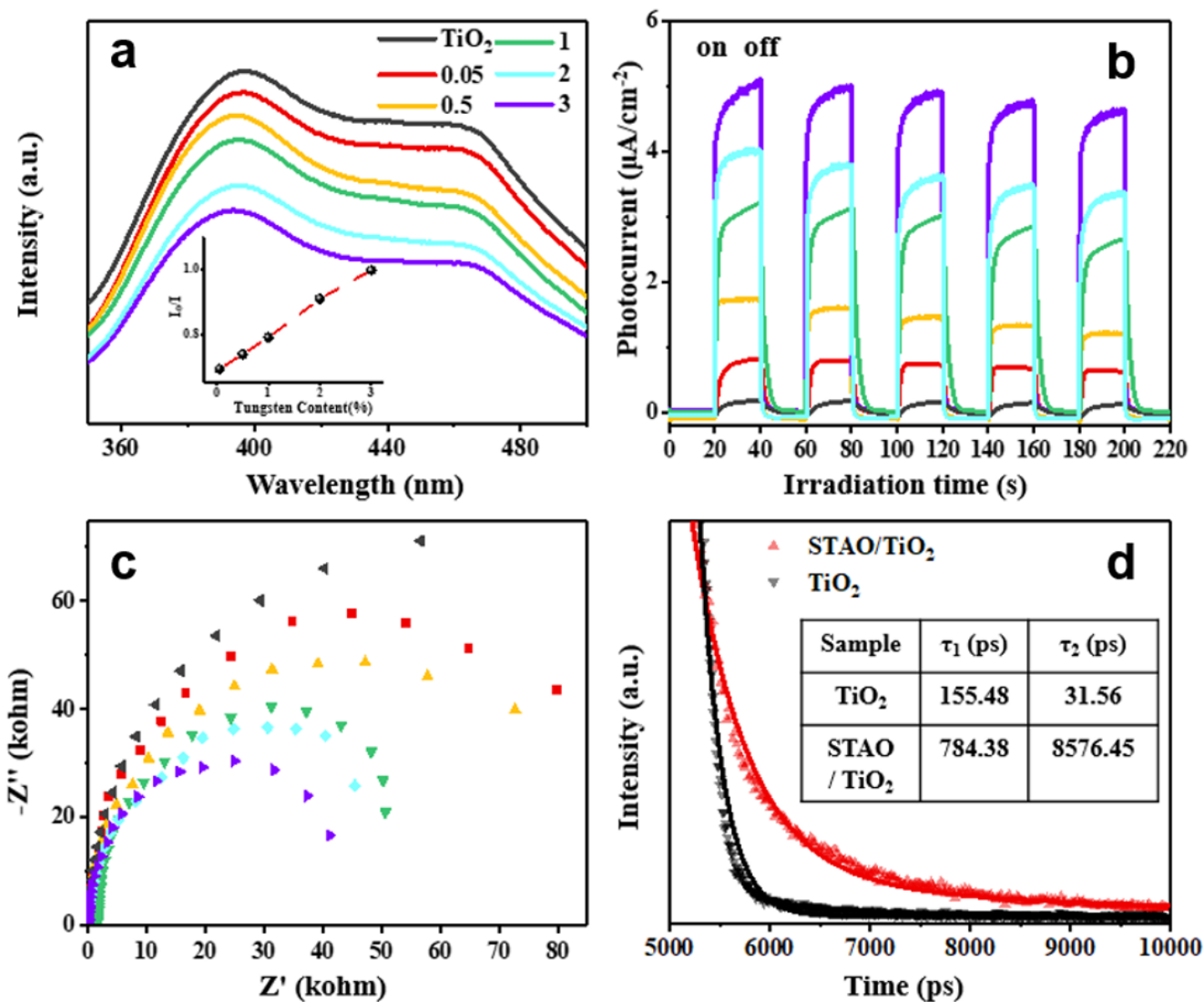


Figure 4

Photocatalytic properties and evolution. a, PL spectra. b, Photogenerated current and c, Nyquist plots of STA0 anchored catalysts with various sites density (0.05-3 wt%). d, Transient time-resolved PL decay spectra of STA0/TiO<sub>2</sub> and pristine-TiO<sub>2</sub>.

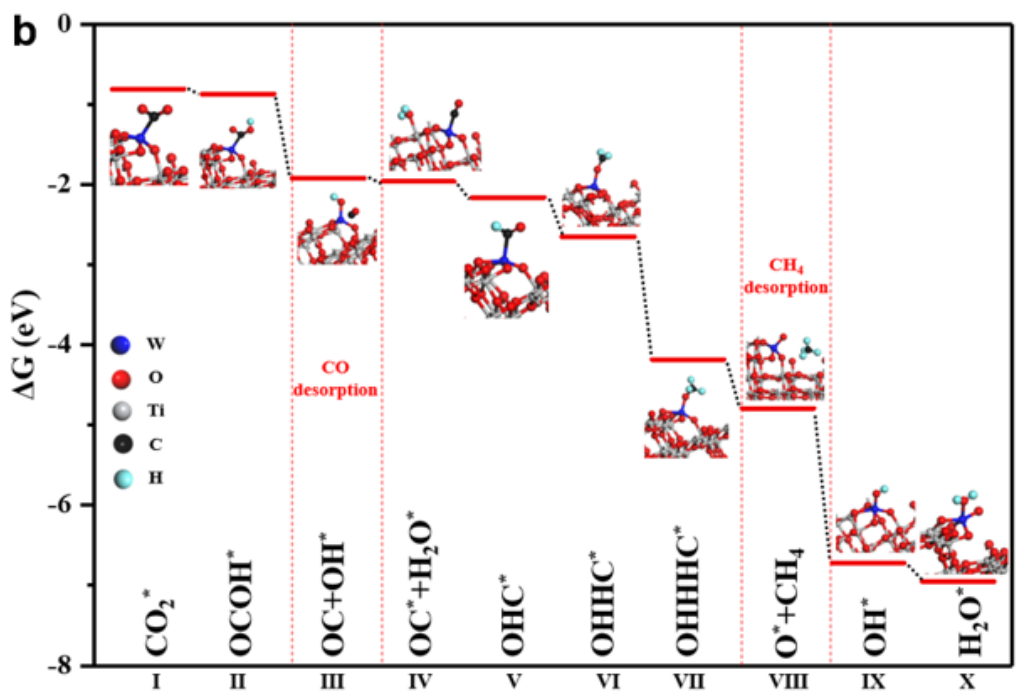
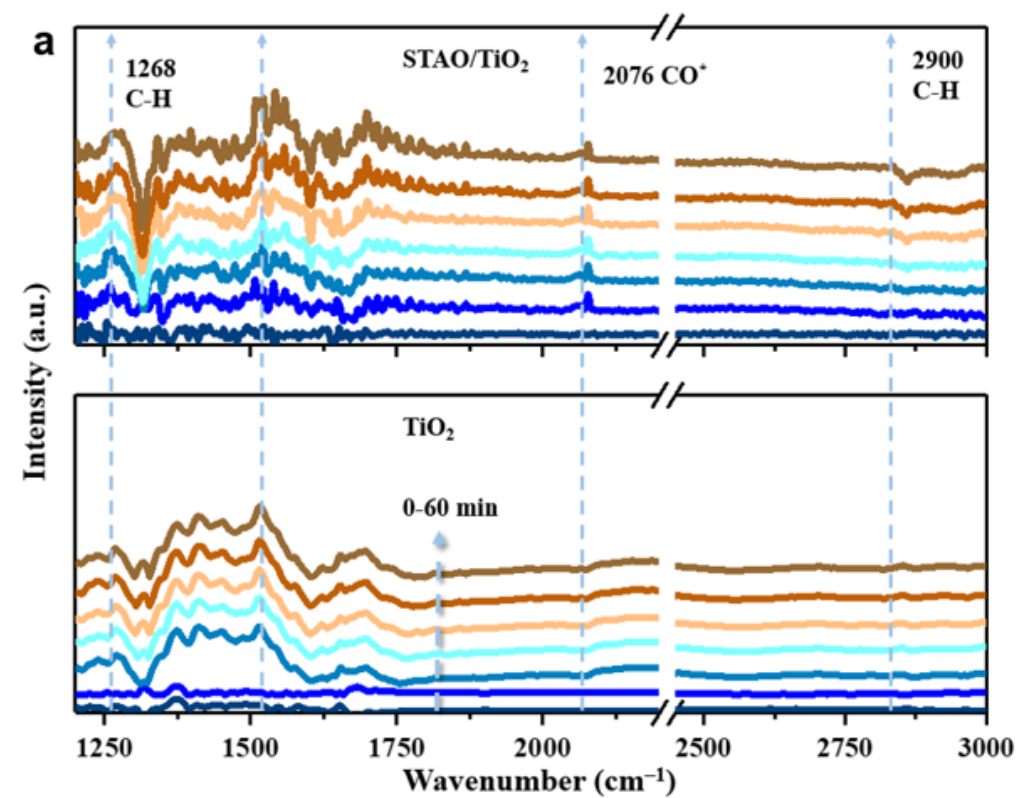


Figure 5

In-situ DRIFTS spectra and DFT simulation of reactive pathway on STA0 at step site. a, DRIFTS signal of STA0/TiO<sub>2</sub> and TiO<sub>2</sub> during photocatalytic CO<sub>2</sub> reduction in 60 mins. b, Reaction pathway from CO<sub>2</sub> to CO and CH<sub>4</sub> on STA0 at step site (step I-X).

## Supplementary Files

This is a list of supplementary files associated with this preprint. Click to download.

- [SupplementaryInformation.docx](#)